

PAPER • OPEN ACCESS

Laser-forged transformation and encapsulation of nanoalloys: pioneering robust wideband electromagnetic wave absorption and shielding from GHz to THz


To cite this article: Shizhuo Zhang *et al* 2024 *Int. J. Extrem. Manuf.* **6** 055501

View the [article online](#) for updates and enhancements.

You may also like

- [Graph networks for molecular design](#)
Rocio Mercado, Tobias Rastemo, Edvard Lindelöf et al.
- [\(Invited\) Hydrogen Is an AWSM Energy Materials Network!](#)
Huyen N. Dinh, Katie Randolph, Adam Z. Weber et al.
- [\(Invited\) The U.S. Department of Energy's Energy Materials Network](#)
Eric L. Miller, Katie Randolph, David Peterson et al.

Laser-forged transformation and encapsulation of nanoalloys: pioneering robust wideband electromagnetic wave absorption and shielding from GHz to THz

Shizhuo Zhang¹, Senlin Rao¹, Yunfan Li², Shuai Wang¹, Dingyue Sun¹, Feng Liu^{1,2,*} and Gary J Cheng^{1,3,*} 

¹ Institute of Technological Sciences, Wuhan University, Wuhan, Hubei 430072, People's Republic of China

² School of Power and Mechanical Engineering, Wuhan University, Wuhan, Hubei 430072, People's Republic of China

³ Purdue University, West Lafayette, IN 47906, United States of America

E-mail: fengliu@whu.edu.cn and gjcheng@purdue.edu

Received 17 October 2023, revised 10 March 2024

Accepted for publication 21 May 2024

Published 1 July 2024



CrossMark

Abstract

The emergence of the internet of things has promoted wireless communication's evolution towards multi-band and multi-area utilization. Notably, forthcoming sixth-generation (6G) communication standards, incorporating terahertz (THz) frequencies alongside existing gigahertz (GHz) modes, drive the need for a versatile multi-band electromagnetic wave (EMW) absorbing and shielding material. This study introduces a pivotal advance via a new strategy, called ultrafast laser-induced thermal-chemical transformation and encapsulation of nanoalloys (LITENS). Employing multivariate metal-organic frameworks, this approach tailors a porous, multifunctional graphene-encased magnetic nanoalloy (GEMN). By fine-tuning pulse laser parameters and material components, the resulting GEMN excels in low-frequency absorption and THz shielding. GEMN achieves a breakthrough of minimum reflection loss of -50.6 dB in the optimal C-band (around 4.98 GHz). Computational evidence reinforces GEMN's efficacy in reducing radar cross sections. Additionally, GEMN demonstrates superior electromagnetic interference shielding, reaching 98.92 dB under THz band (0.1–2 THz), with the mean value result of 55.47 dB. These accomplishments underscore GEMN's potential for 6G signal shielding. In summary, LITEN yields the remarkable EMW controlling performance, holding promise in both GHz and THz frequency domains. This contribution heralds a paradigm shift in EM absorption and shielding materials, establishing a universally applicable framework with profound implications for future pursuits.

* Authors to whom any correspondence should be addressed.



Original content from this work may be used under the terms of the [Creative Commons Attribution 4.0 licence](https://creativecommons.org/licenses/by/4.0/). Any further distribution of this work must maintain attribution to the author(s) and the title of the work, journal citation and DOI.

Supplementary material for this article is available [online](#)

Keywords: laser processing, multivariate metal–organic frameworks, electromagnetic wave absorption

1. Introduction

In recent decades, there has been an unprecedented surge in wireless communication technology, leading to significant societal changes across various domains [1, 2]. Within this wireless communication landscape, the deployment of electromagnetic waves (EMWs) across various frequency bands is tailored to specific applications, collectively shaping the fabric of the network of wireless communication [3, 4]. The evolution is exemplified by the ongoing development of sixth-generation (6G) communication standards following the commercial realization of 5G standardization. Anticipated to exhibit data transfer rates 100 times those of prevailing standards [5, 6], 6G technology represents a notable shift, marked by the incorporation of terahertz (THz) waves—those exceeding 100 GHz frequency—proffering boundless prospects for high precision and ultrafast internet of things applications [4, 6–8]. However, existing communication systems, such as satellite communications, frequently employ low-frequency EMWs (S-band and C-band) due to their wide signal coverage and robust penetration capabilities. Thus, it can be implied that the convergence of gigahertz (GHz) and THz will be future wireless communication trend [9, 10]. Accordingly, the imperative arises for versatile electromagnetic materials simultaneously effective in both GHz and THz domains [11, 12]. Notwithstanding, prevailing challenges necessitate meticulous consideration prior to their practical realization.

A central challenge lies in achieving high magnetic component dispersion in wave-absorbing materials within conventional preparation procedures, often resulting in suboptimal low-frequency EMW absorption [9, 13, 14]. Similarly, the realm of THz EMW shielding remains limited, hampering the establishment of mass-processable materials exhibiting remarkable shielding performance [15]. These limitations of material and processing technique greatly limit the application of future communication mode. Consequently, the development of materials proficient in low-frequency EMW absorption and THz shielding, coupled with a universally applicable processing technique, emerges as a critical endeavor.

As new types of multifunctional materials, metal–organic frameworks (MOFs) are synthesized via coordination bonding between metallic ions and organic ligands, exhibiting some unique physical attributes [16–18]. These attributes have underpinned their extensive utilization in catalysis, gas separation, and beyond [19]. Within the domain of EMW absorption, MOFs have paved the way for the development of porous carbon-based derivatives [16, 17, 20], endowed with benefits including reduced density, elevated mechanical strength,

and robust stability—qualities conducive to absorber density reduction [21]. Moreover, carbon-based MOF derivatives manifest high electron conductivity, fostering pronounced resistance loss and effective electromagnetic shielding within the THz band [22, 23]. By leveraging the transition of metal ions within MOFs to their reduced counterparts—metal oxides or nanoparticles—via multivariate MOFs (MTV-MOFs), the resulting carbonized MTV-MOFs derivatives effectively mitigate the limitations associated with single-component material loss mechanisms, thereby optimizing absorber impedance matching conditions [24, 25].

Present MOF carbonization processes, involving high-temperature calcination or solvent-based methods, are characterized by intricate procedures, substantial energy and solvent consumption. For instance, Wu *et al* synthesized a binary MOF-based hybrid nanoflowers via magnetic stirring reaction for 18 h with high temperature [26]. Liu *et al* introduced Mn-Based MOFs-derived composites using solvothermal method with 105 °C for 20 h [27]. Similarly, Ouyang *et al* reported the carbonizing MOF-74 derivatives by solvothermal method with 120 °C for 24 h [28]. In the same way, Yi *et al* prepared the Co-based PBA with a long reaction under 500 °C–900 °C [29]. By contrast, laser-based processing presents advantages of rapidity, convenience, and simplicity, offering potential for large-scale preparation. For instance, in comparison to lengthy high-temperature tubular furnace reactions, lasers enable swift high-temperature reactions. Laser parameters can be adeptly adjusted to regulate the degree of graphitization, influencing conductive loss, while also precisely modulating thermal-chemical reduced nanoalloy particle sizes, achieving nano-scale preparation with favorable dispersity. Consequently, the laser chemical inducing method excels in dispersing nanoalloys into carbon matrices, enhancing extensive interfacial loss and optimizing the magnetic and dielectric loss within low-frequency regimes matching [30].

Within this context, this paper represents significant strides towards the realization of high-performance EMW absorbers and shields via laser-induced thermal-chemical transformation and encapsulation of nanoalloys (LITENs). A high-efficiency method to mass-produce graphene-encased magnetic nanoalloys (GEMNs) via LITEN has been introduced, offering simplicity, stability, and parameter adjustability that holds promise for broader absorber applications. Moreover, the electromagnetic response characteristics of GEMN have been systematically analyzed, encompassing low-frequency microwave absorption, THz shielding, and radar cross-section (RCS) reduction. Under laser-customized impedance matching, the GEMN(Fe/Co/Ni) synergistically exhibited exceptional EMW absorption. Remarkably, the

Fe/Co/Ni nanocomposites attained a minimum reflection loss (RL_{\min}) of -50.6 dB at a remarkably low frequency of 4.98 GHz. In the THz domain, GEMN's electromagnetic interference (EMI) shielding excelled, yielding values of up to 98.92 dB, with an average shielding of 55.47 dB spanning 0.1 – 2 THz. These findings unequivocally demonstrate GEMN's efficacy as an electromagnetic coupling trap, paving the way for high potential in the forthcoming era of wireless communication.

2. Result and discussion

Figure 1(a) provides an illustrative representation of the LITEN process underlying the laser thermal-chemical transformation of graphene encased magnetic nanoalloys. This procedure involves the application of pulse laser-induced thermal chemical transformation, which instantaneously pyrolyzes Fe/Co/Ni MTV-MOF crystals, culminating in the creation of a porous graphene foam encapsulating magnetic nanoalloys. The native MTV-MOF crystals encompass terephthalic acid as the linker and $Ni^{2+}/Co^{2+}/Fe^{2+}$ as central nodes (figure 1(c)). Following laser treatment, the terephthalic acid transforms into a porous graphene structure, concurrently facilitating the conversion of ions into their respective nanoalloy forms, encased within the graphene matrix to thwart oxidation. Specifically, the detailed LITEN process can be broken down into several processes. With the laser energy absorbed by the MTV-MOF, it forms high temperature and high pressure at localized position within one pulse inside the slide. Upon this extreme manufacturing situation, the isolated MOF crystals were instantly pyrolyzed by thermochemical pyrolysis. The organic species were reorganized to form a 3D graphene skeleton while laser forged, while the reduced Fe/Co/Ni atoms gathered to form nanoalloy and buried in the graphene skeleton. In addition, the plasma produced by laser ablation propels the precursor in GEMN, which achieves an even and homogeneous reaction. Ultimately, the organic linkers undergo complete pyrolysis, resulting in the formation of a porous graphene foam housing embedded magnetic constituents. Capitalizing on its robust electrical conductivity and magnetic coupling properties, GEMN functions as an EMW trap (figure 1(b)), poised to excel in GHz absorption and THz electromagnetic shielding and absorption applications.

The discussion engendered by this fabrication process underscores its potential significance in various technological applications. The utilization of LITEN for the synthesis of GEMNs presents a novel avenue in material engineering. This method's precision in controlling the conversion of MOF components into tailored nanoalloys while concurrently generating a graphene foam structure offers unique advantages. By preventing metal oxidation and effectively integrating the magnetic constituents within the graphene matrix, the resulting GEMN possesses an optimal structure for EMW manipulation. Moreover, the introduced reductive atmosphere during the process contributes to enhancing the stability and performance of the resultant material. Furthermore, the adaptability of

the LITEN renders it amenable to scalability and mass production. Compared to conventional techniques with prolonged reaction times and energy-intensive steps, this method's rapid and controlled thermal event is advantageous for large-scale material preparation. The ensuing GEMN's robust potential as an EMW trap, capable of simultaneous GHz absorption and THz electromagnetic shielding and absorption, holds implications for a wide spectrum of technological fields including wireless communication, sensing, and electronic warfare.

The meticulously delineated fabrication process through LITEN represents a significant advancement in material synthesis. This process harnesses the unique properties of MOFs, graphene, and nanoalloys to yield a multifunctional material with remarkable potential for transformative applications. The interplay between reductive environments, precise thermal control, and structural integration elucidates the promise of this method for shaping the future of EMW manipulation technologies. In this study, we employed $(Ni_2Co)_1-xFex$ -MOF-NF [31] as a representative example for the facile and cost-effective preparation of GEMN via LITEN, exemplifying the adaptability and potential of this method. The modularity of the metal ion ligands in terms of elements and content ratios offers a customizable framework, thereby enabling optimization of the absorber's impedance matching. The MTV-MOF was further scrutinized by scanning electron microscopy (SEM), revealing a 3D foam-like architecture composed of interconnected nanofibers (figures 1(d) and S1). Subsequent laser treatment led to the complete pyrolysis of the foam-like MOF into a porous 3D graphene foam (figure 1(e)). With the laser power of 4.56 W, the penetration depth of the MOF can be 30 μm (figure S2). According to the SEM image in figure S3, it can be figured out that the organic ligands are more easily carbonized, meanwhile the metal ions are also easily reduced to larger nanoparticles. Hence, by controlling the laser parameter, the dielectric constant and permeability of the absorbing material can be effectively matched. This carbonaceous material displayed pronounced resistance loss characteristics, accompanied by the observation of cavities within GEMN, which assume the role of EMW traps, thereby enhancing wave refraction and absorption.

The magnetic nanoalloys, generated via thermal reduction, became embedded within the porous graphene matrix (figure S4), functioning as magnetic loss agents akin to bamboo thorns in the EMW trap. Notably, the Fe/Co/Ni nanoalloy, driven by the ferromagnetically enhanced Kirkendall diffusion effect, exhibited confinement within a core-shell structure, effectively thwarting magnetic agglomeration. Consequently, magnetic nanoalloys, ranging around 100 nm, were clearly discernible within the foam-like architecture [14, 32]. Additionally, a substantial population of sub- 10 nm alloy particles was found to be distributed upon the graphene layer (figure 1(f)).

Transmission electron microscopy (TEM) analysis of GEMN has provided valuable insights into the material's structural characteristics and the uniformity of its magnetic nanoalloy nanoparticles, as illustrated in figure 1(g). This examination following laser-induced thermal-chemical processes revealed the successful generation of uniformly

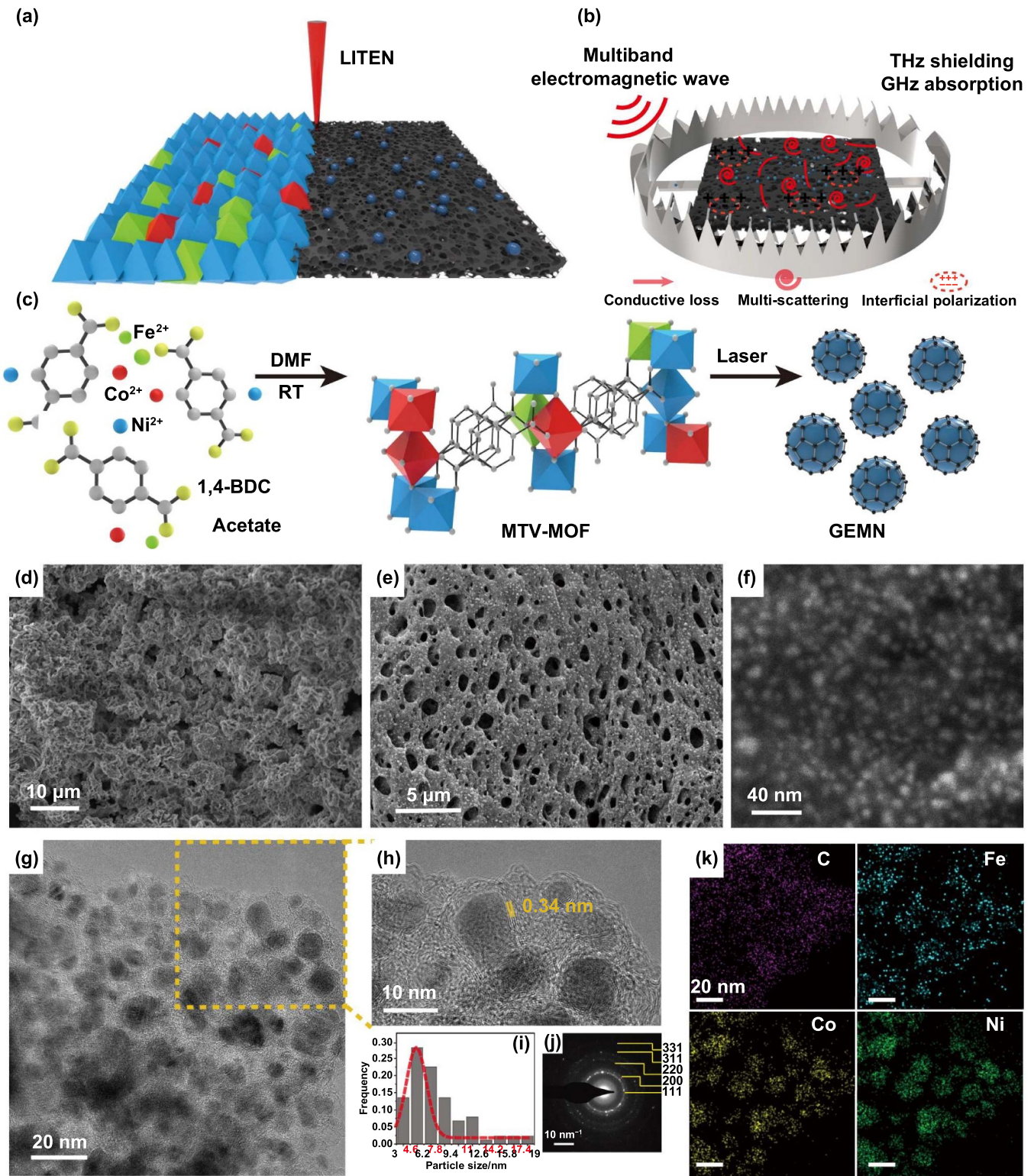


Figure 1. LITEN induced graphene-encased magnetic nanoalloys (GEMNs). (a) Schematic of the LITEN for preparing GEMNs. (b) The application schematic of GEMN 'trap' in low-frequency band electromagnetic wave absorption and terahertz electromagnetic shielding. (c) Schematic illustrations of the process of preparing GEMN. (d) SEM image of the Fe/Co/Ni MTV-MOF. (e) SEM image of the GEMN. (f) The high magnifications SEM image of magnetic nanoalloy on graphene layer. (g) TEM image revealed that the magnetic nanoalloy was distributed on graphene layer. (h) Local magnification image of the GEMN. (i) The particle size distribution of magnetic nanoalloy nanoparticles. (j) The SAED pattern of GEMN. (k) Elemental distribution mapping of C/Fe/Co/Ni nanocomposites.

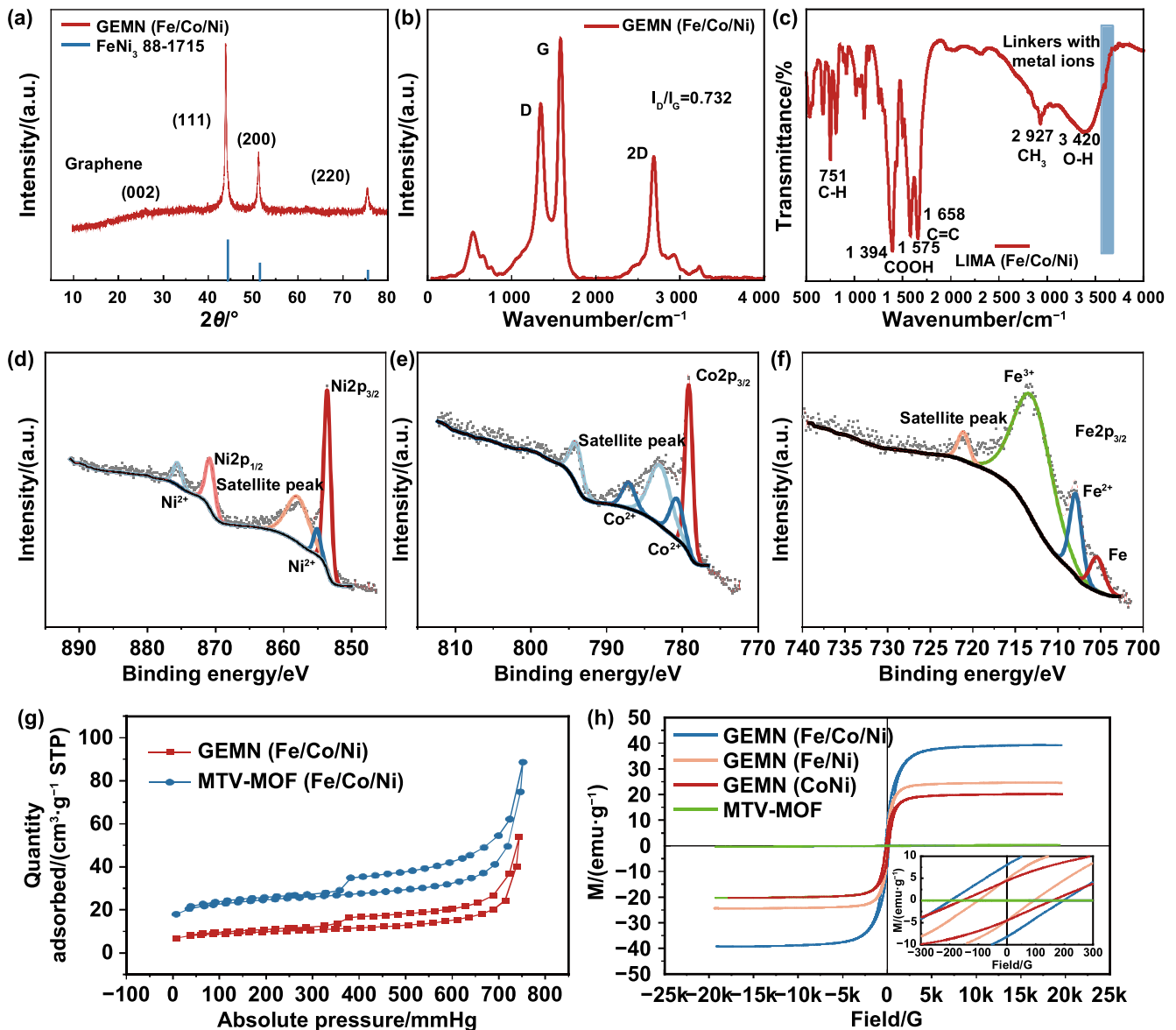


Figure 2. The characterization of the GEMNs. (a) XRD of GEMN. (b) Raman spectra of GEMNs under nanosecond laser. (c) The FTIR of the GEMN. The XPS analysis of (d) Ni 2p, (e) Co 2p, and (f) Fe 2p spectrums of the GEMN. (g) The BET of the GEMN and the corresponding MTV-MOF. (h) Room temperature magnetic hysteresis loops of GEMN under different compositions.

dispersed nanoparticles. The utilization of pulse laser-induced thermionic reduction contributed to the enhanced uniformity in particle distribution. Statistical data from the analysis demonstrated that the synthesized magnetic nanoalloy particles exhibited a normal particle distribution ranging from 3 nm to 19 nm, with an average value of approximately 6.2 nm (figure 1(i)). Furthermore, the selected area electron diffraction (SAED) image presented in figure 1(j) exhibited the distinct electron diffraction pattern, providing clear evidence that the graphene-encased Fe/Co/Ni ternary alloys consisted of multiple crystalline nanoparticles. This crystallinity underscores the robustness and stability of the synthesized nanomaterial, further supporting its suitability for various applications.

Moreover, energy dispersive x-ray spectroscopy (EDS) mappings (figures 1(k) and S5) conducted on the graphene

surface displayed a consistent and uniform distribution of all metallic elements. This distribution aligns with the findings from EDS spectra observed via SEM (figure S6). The uniform elemental distribution is crucial as it ensures the homogeneity of the material's electromagnetic properties, particularly its ability to interact with EMWs. This analysis not only confirms the uniformity and metallic nature of the magnetic nanoalloy nanoparticles within GEMN but also provides a structural basis for its excellent electromagnetic properties. The uniform distribution and crystalline nature of the nanoparticles are key factors contributing to GEMN's performance in electromagnetic applications.

In figure 2(a), the XRD pattern of a GEMN (Fe/Co/Ni) is presented. There is a distinct peak at 26.36° corresponding to the (002) crystal plane of graphene [33], while the features of 44.193° , 51.441° , and 75.759° arise from (111),

(200), and (220) crystallographic planes of Fe/Co/Ni with a face-centered cubic structure, indicative of alloy formation [34]. This observation underscores the successful incorporation of Fe/Co/Ni alloy within the trimetallic samples. The morphological analysis reveals the encasement of nanoalloys within the graphene layer. Graphene formation is further confirmed by the Raman spectra at 1339 cm^{-1} , 1583 cm^{-1} , and 2688 cm^{-1} (figure 2(b)), which corresponds to the D/G/2D peaks [24]. This outcome remains consistent when employing femtosecond laser irradiation (figure S7). The relative peak intensity (ID/IG) ratio in the Raman spectrum suggests graphene formation under distinct laser pulse widths. Notably, TEM images of the graphene shell indicate predominantly 3–7 layers of graphene (figure S8). With nanosecond lasers yielding heightened thermal effects, an increase in defect generation is observed. The GEMN exhibits significant electrical conductivity facilitated by its graphene-based conductive network. Electrical conductivity measurements under varying laser powers (figure S9) reveal optimal results at 4.56 W, indicative of the material's substantial potential for conductivity-related EMW absorption.

Furthermore, Fourier-Transform Infrared (FTIR) analysis of GEMN and corresponding Fe/Co/Ni MOF samples (figures 2(c) and S10) provides insights into chemical changes of post-laser processing. The appearance of characteristics at 3420 cm^{-1} , 1575 cm^{-1} , 1394 cm^{-1} , and 751 cm^{-1} come down to the tensile vibration of O–H, the vibration of COOH, and the bending vibration of the carbon hydrogen bond in the benzene ring, respectively. The vanish of the sharp characterization of 3606 cm^{-1} post-laser treatment signifies the breakdown of metal ion coordination and the formation of the nanoalloy.

Surface element analysis and the assessment of their valence states within GEMN(Fe/Co/Ni) were conducted using x-ray photoelectron spectroscopy (XPS). The comprehensive XPS spectrum (figure S11) revealed the Fe, Co, Ni, C, and O elements within in GEMN sample. The emergence of oxygen (O) can be ascribed to defects within the graphene structure, and the formation of oxygen-containing groups inside of the sample. A more particular examination of the valence states of Fe, Co, and Ni was carried out through Fe 2p, Co 2p, and Ni 2p XPS spectra, as depicted in figures 2(d)–(f), respectively. In the Ni 2p spectrum, it can be observed that two prominent peaks located 853.6 eV and 870.9 eV unequivocally confirm the metallic state of Ni atoms. Additionally, the peaks located at 861.6 eV and 879.7 eV indicate the presence of Ni^{2+} within the Fe/Co/Ni alloys, with an evident satellite peak located at 858.2 eV . A similar analysis of the Co 2p spectrum reveals a prominent peak at 779.2 eV , affirming the metallic state of Co. Furthermore, the binding energies at 780.9 eV and 787.2 eV signify the presence of Co^{2+} , accompanied by a satellite peak at 783.1 eV and another at 794.1 eV . Regarding the Fe element, a peak at 705.6 eV confirms its metallic state, while characteristic peaks at 707.9 eV and 713.5 eV correspond to Fe^{2+} and Fe^{3+} . Collectively, these results provide compelling evidence for the successful formation of distinct Fe/Co/Ni alloy phases within the GEMN structure. This detailed surface analysis underscores the precise control achieved in fabricating

the desired alloy compositions, which is of paramount importance in tailoring the electromagnetic properties of the material for specific applications.

Nitrogen sorption tests were conducted to assess the properties of both GEMN and Fe/Co/Ni MTV-MOF, with the corresponding results presented in figure 2(g). Furthermore, the distribution of pore size was determined through the BJH method, as depicted in figure S12. Notably, the Fe/Co/Ni MTV-MOF exhibited a substantial Brunauer–Emmett–Teller (BET) surface area of $86.218\text{ cm}^3\cdot\text{g}^{-1}$. However, following laser treatment, the BET surface area notably decreased to $33.257\text{ cm}^3\cdot\text{g}^{-1}$. The distinction in BET surface area can be further elucidated by analyzing the pore size distribution. The MOF material inherently comprises a distributed array of micropores, which, under the influence of laser treatment, undergo carbonization and crosslinking processes. Consequently, it can be observed that the BET surface area of GEMN is diminished when compared to the original MOF material.

For an in-depth evaluation of the GEMN samples, VSM hysteresis loops further recorded the magnetic properties of the sample. According to the result of figure 2(h), both GEMN samples, encompassing Fe/Co/Ni, Fe/Ni, and Co/Ni nanocomposites, demonstrated saturation magnetization (M_s) values of approximately $39.33\text{ emu}\cdot\text{g}^{-1}$, $24.65\text{ emu}\cdot\text{g}^{-1}$ and $20.26\text{ emu}\cdot\text{g}^{-1}$, respectively. Furthermore, an additional magnetic property is revealed in the inset of figure 3(i), where coercivity (H_c) values were determined to be approximately 199.96 Oe for Fe/Co/Ni, 159.61 Oe for Fe/Ni, and 100.07 Oe for Co/Ni nanocomposites, respectively. The variation in H_c results arises from the difference of components in GEMN, and the distribution of defects induced by laser treatment. According to the principles of ferromagnetic resonance theory, it is discerned that larger H_c values contribute to an enhanced EMW absorption performance, particularly at high frequencies.

In EMW absorption research, it is widely recognized that an RL value below -10 dB corresponds to the effective absorption of EMWs, thereby defining this effective absorption bandwidth (EAB). In the context of this study, the RL values of GEMN with varying elements were assessed at 25 wt% loadings (figures 3(a)–(c)). The intricate contour maps of 3D-RL curves across frequency and thickness variations are displayed in figures 3(a)–(c). A notable observation is the remarkable EMW absorption performance exhibited by GEMN(Fe/Co/Ni), which outperforms other samples. Specifically, the RL_{\min} value of -50.6 dB is attained at 4.98 GHz frequency, resulting in an EAB spanning 3.92 GHz . Conversely, under the same loading ratio, the bicomponent samples (Ni/Fe and Ni/Co) demonstrate inferior absorption performance due to inadequate impedance matching.

The quarter wavelength ($1/4\lambda$) matching model has been widely used to evaluate the result between the frequency of RL_{\max} and the matched thickness (t_m) of an air-absorber can be expressed as: $t_m = n\lambda/4 = nc/4f_m\sqrt{\mu_r\epsilon_r}$ ($n = 1, 3, 5, \dots$), in which λ denotes the wavelength of EMW and c denotes the speed of light. In line with the experimental results presented

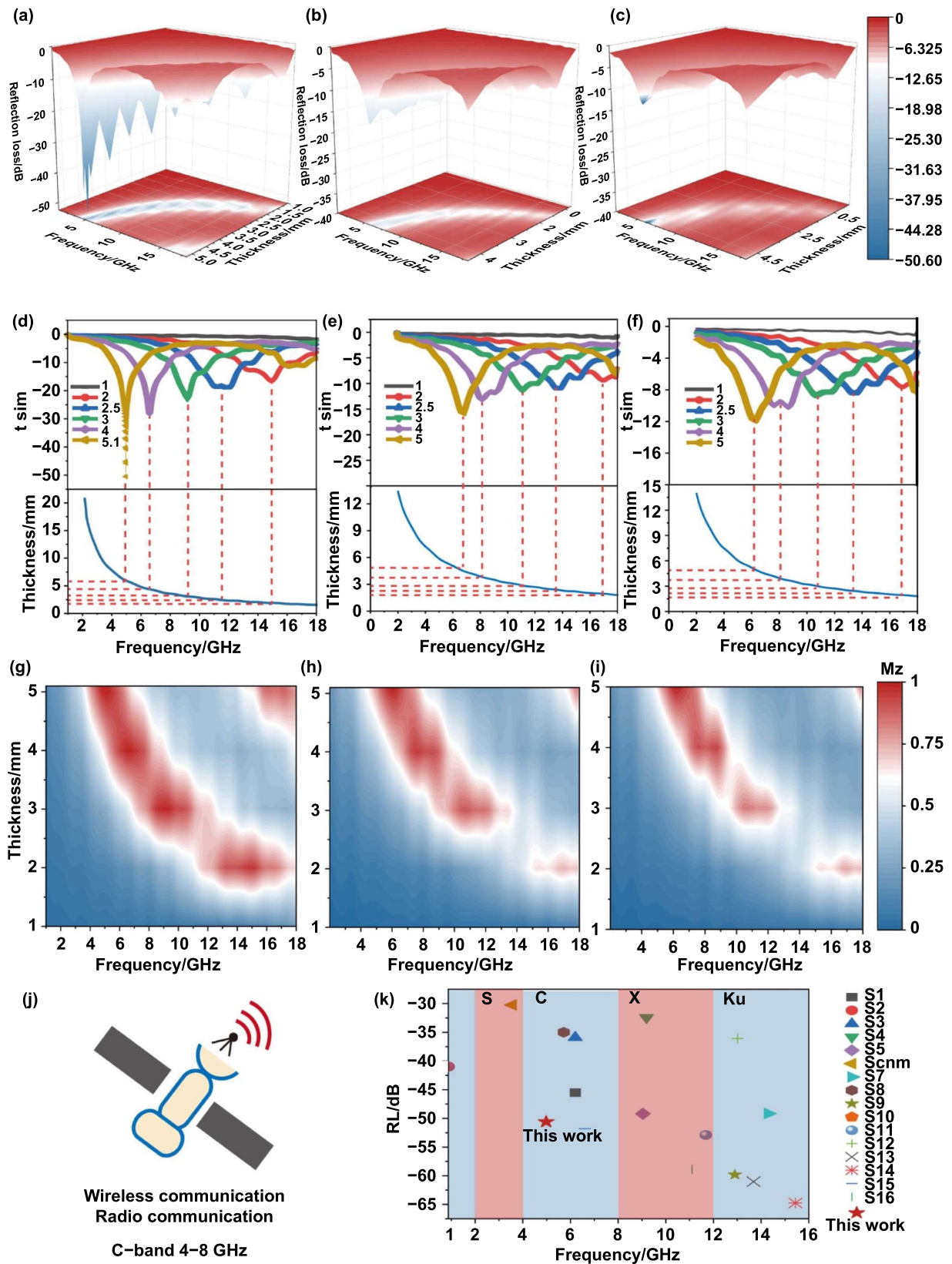


Figure 3. The calculated reflection loss properties diagram and the theoretical matching of the GEMN. The 3D RL curve and reflection loss map presentations of the (a) GEMN(Fe/Co/Ni), (b) GEMN(Fe/Ni), and (c) (Co/Ni). The RL curves and the simulation results under different thicknesses (d) GEMN(Fe/Co/Ni), (e) GEMN(Fe/Ni), (f) (Co/Ni). And the Z-values of two-dimensional shadows under different thicknesses and frequencies of (g) GEMN(Fe/Co/Ni), (h) GEMN(Fe/Ni), (i) (Co/Ni). (j) Schematic of C-band application in wireless communication. (k) The microwave absorption performance comparison of GEMN with the other MOF-derivatives.

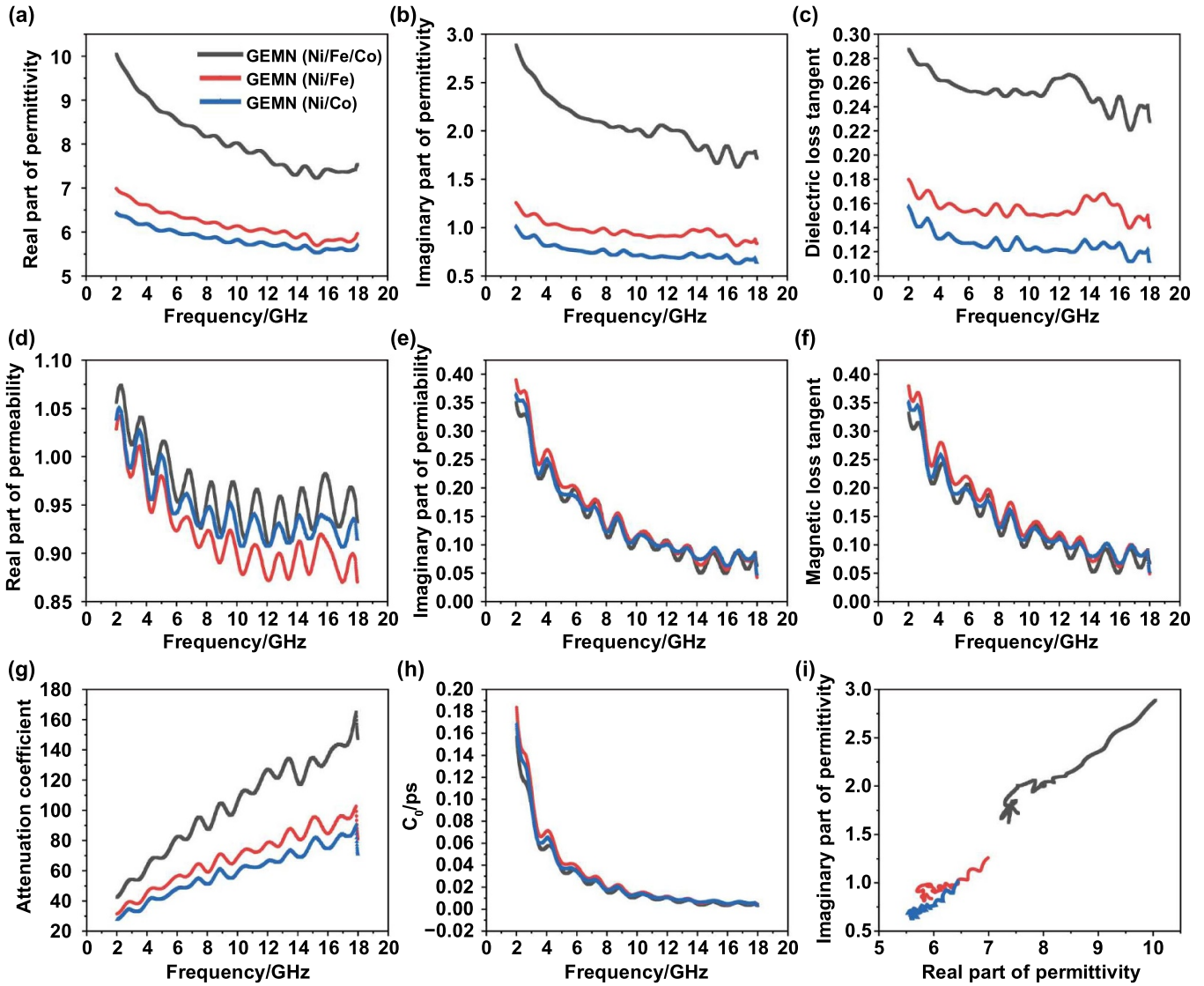


Figure 4. The electromagnetic parameters of GEMN(Fe/Co/Ni), GEMN (Fe /Ni), GEMN (Co/Ni) (a) and (b) complex permittivity, (c) the tangent ε , (d) and (e) complex permeability, (f) the tangent μ . (g) Attenuation coefficient, (h) the C_0 curves, and (i) Cole–Cole semicircles.

in figures 3(d)–(f), the experimentally determined t_m (corresponding to RL_{\min}) exhibits commendable consistency with the simulated values. These findings substantiate the agreement of GEMN’s absorption curve with the $\lambda/4$ destructive interference model. Furthermore, impedance matching is a pivotal determinant of air-absorber performance. For the traditional impedance matching theory, a value of normalized characteristic impedance modulus ($Z = |Z_{in}/Z_0|$) approaching 1 signifies better impedance matching [35]. Correspondingly, as shown in figures 3(g)–(i), the RL_{\min} of GEMN tends to align with Z values near 1, which represents the well impedance matching under this frequency/thickness. Combining EMW loss mechanism with impedance matching theory, the GEMN realized a better frequency matching [36].

The C-band EMW is characterized by attributes such as extensive propagation distance, strong penetration, robust anti-interference capabilities, and heightened accuracy and resolution (figure 3(j)). Nevertheless, common absorbers often

present optimal matching bands in high-frequency ranges, limiting effective electromagnetic absorption within the C-band. Consequently, employing the thermal-chemical inducing strategy, GEMN achieves superior dispersion of magnetic components (figure 3(k)), thereby demonstrating excellent low-frequency band matching and absorption performance, which holds potential significance for C-band applications.

The electromagnetic parameters of GEMN are elucidated in figure 4. The real part (ε' , μ') and the imaginary part (ε'' , μ'') of these parameters correspond to the storage and dissipation mechanisms of EMWs, respectively. Within the low-frequency range, both real part (ε') and imaginary part (ε'') exhibit comparable descending trends. This behavior is evident from figure 4(a), wherein the ε' values of GEMN (Fe/Co/Ni, Fe/Ni, and Co/Ni) range from 10.04 to 7.54, 6.99–5.96, and 6.44 to nearly 5.71, respectively. The ε'' values of GEMN (Fe/Co/Ni, Fe/Ni, and Co/Ni) span from 2.88 to 1.71,

2.01–0.83, and 1.01–0.65 (figure 4(b)). Notably, the consistent alteration tendencies in real part (ϵ') and imaginary part (ϵ'') across all samples suggest a shared dielectric loss mechanism (figures 4(a) and (b)). Furthermore, the presence of multiple evident fluctuation peaks in ϵ'' curves indicates the occurrence of polarization relaxation behavior. This phenomenon effectively augments the EMW absorption performance.

The $\tan\delta\epsilon = \epsilon''/\epsilon'$, denoting the actual dielectric loss capability, is depicted in figure 4(c). It becomes evident that GEMN(Fe/Co/Ni) showcases a stable loss performance across 2–18 GHz. In comparison to the binary alloy counterparts, the Fe/Co/Ni sample yields the highest $\tan\delta\epsilon$ value across this scope. The complex permeability of GEMN samples is delineated in figures 4(d) and (e), revealing a serpentine-shaped decrease in response to increasing frequency. This serpentine pattern signifies the multiple resonances of dielectric loss occurring within the absorber's interior. Due to the small particle size and high dispersion of GEMN, μ'' exhibits a high value in the low-frequency band. As a result, these samples exhibit multiple magnetic loss mechanism [36, 37]. The variation trends of $\tan\delta\mu$ ($\tan\delta\mu = \mu''/\mu'$) portray that GEMN (Fe/Co/Ni) and GEMN (Fe/Ni) exhibit the highest $\tan\delta\mu$ (0.19–0.26) and the lowest $\tan\delta\mu$ (0.05–0.12), respectively. By comparing the $\tan\delta\epsilon$ (figure 4(c)) and $\tan\delta\mu$ (figure 4(f)) curves of these samples, the $\tan\delta\mu$ and $\tan\delta\epsilon$ are nearly matching under low frequency band, and $\tan\delta\mu < \tan\delta\epsilon$ in the high frequency region. These findings collectively underline GEMN's capacity to harbor multiple magnetic/dielectric loss mechanisms for effective dissipation.

The attenuation coefficients (α) displayed in figure 4(g) demonstrate similar trends among all samples across a broad frequency range. Carbon-based components bestow excellent attenuation capabilities, with observed differences attributed to previously analyzed impedance matching variations. In contrast to the distinct components, while the attenuation coefficients of GEMN remain akin, GEMN(Fe/Co/Ni) surpasses the other bicomponent samples. Magnetic losses can be specifically divided into hysteresis losses, eddy current losses, and multi-source resonance losses. The C_0 value is commonly employed to study the loss mechanism, and a consistent C_0 value suggests eddy current loss as primary magnetic loss way. However, as figure 4(h) illustrates, with the C_0 value fluctuating, it can be referenced the eddy current loss is not the principal contributor. Consequently, GEMN samples exhibit not only eddy current loss but also capabilities for natural resonance and exchange resonance losses.

The Cole–Cole semicircle (figure 4(i)) corresponds to Debye dipole relaxation process, while the extension curve corresponds to conductive loss. In this context, distorted semicircles observed in GEMN samples suggest the multiple loss mechanism of GEMN. The interfacial polarization relaxation arises from uneven charge distribution at defects and interfaces between nanoalloys and graphene, while the dipolar relaxation is attributed to functional groups like C=O and C–O. The high carbon content in both samples results in straight-line behavior, indicating high conductive loss.

Figure 5 encapsulates and elucidates the intricate EMW absorption mechanisms underpinning the GEMN. To elucidate further, the laser-induced graphene's porous conductive framework was pivotal in establishing a heightened capacity for conductive loss within the nanocomposites. The internal porous structure of GEMN enhances the multiple scattering of EMWs within the material, thereby enhancing the electromagnetic absorption of the material. Moreover, the profusion of interfaces between graphene, Ni, Fe and Co potentiated augmented interfacial polarization. Meanwhile, the defects in the GEMN present within the structure also facilitated dipole polarization effects.

Additionally, the introduction of magnetic nanoalloys introduced the dimension of natural resonance, thereby further amplifying the EMW attenuation prowess. Finally, by adeptly tailoring the impedance match between the graphene and the magnetic alloy nanoparticles, the composite GEMN proficiently permitted the efficient penetration of EMWs. To conclude, an insightful arrangement of component composition and microstructural design within laser-induced MOF-derived nanocomposites coalesced to yield a superlative EMW absorption performance. This intricate comprehension highlights the fusion of various mechanisms that contribute to the exceptional absorptive attributes demonstrated by the GEMN structure.

In the domain of microwave absorption materials, the RCS assumes a pivotal role as a direct assessment metric within practical stealth technology scenarios. Specifically, RCS quantifies the intensity of the echo generated by a target when subjected to radar wave irradiation. It represents the effective area of the target and is symbolized by the projected area of an equivalent reflector that possesses uniformity in all directions. Consequently, lower values signify enhanced absorption performance. In this context, we conducted RCS simulations for the GEMN absorber using CST simulation software. The simulation model, as depicted in figure 6(a), entailed the placement of the absorber atop a perfectly electrically conducting (PEC) layer. The incident wave approached from the negative direction of the absorber plane, with θ representing the angle of incidence in the simulation setup. Comparative visualizations of the PEC sample and GEMN under varying thetas are showcased in figure 6(b). Clearly discernible is the diminished signal strength of the GEMN/PEC absorber in contrast to the PEC sample, with all RCS values for GEMN/PEC registering lower than $-10 \text{ dB}\cdot\text{m}^{-2}$. Further insight into the two-dimensional RCS values of the PEC and GEMN/PEC, across distinct incident angles, is presented in figures 6(c) and (d). These values correspond substantively with the exceptional microwave absorption performance previously discussed. A contrast of the radar maps post-absorption, as illustrated in figure 6(e), underscores the GEMN's capacity for reducing the scattering and reflection of EMWs emanating.

THz waves have attracted great attention due to the immense potential in the realm of 6G wireless communication. However, the development of THz waves caused a surge

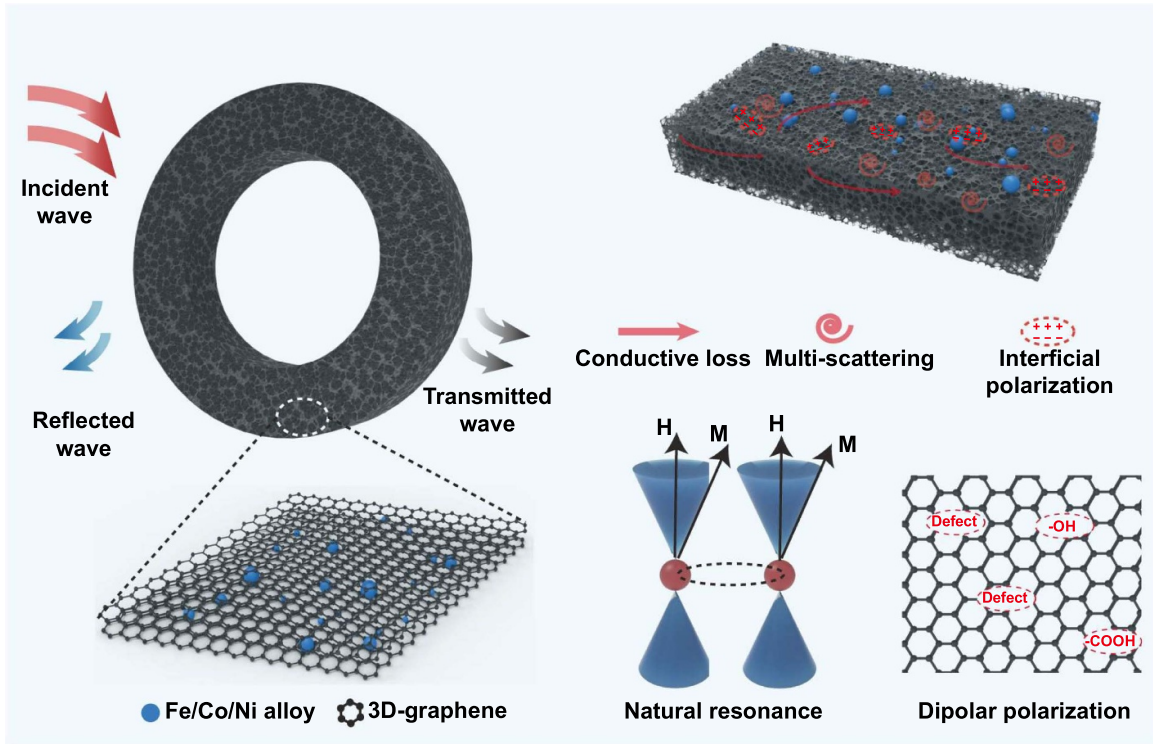


Figure 5. Schematic mechanisms of microwave absorption in GEMN.

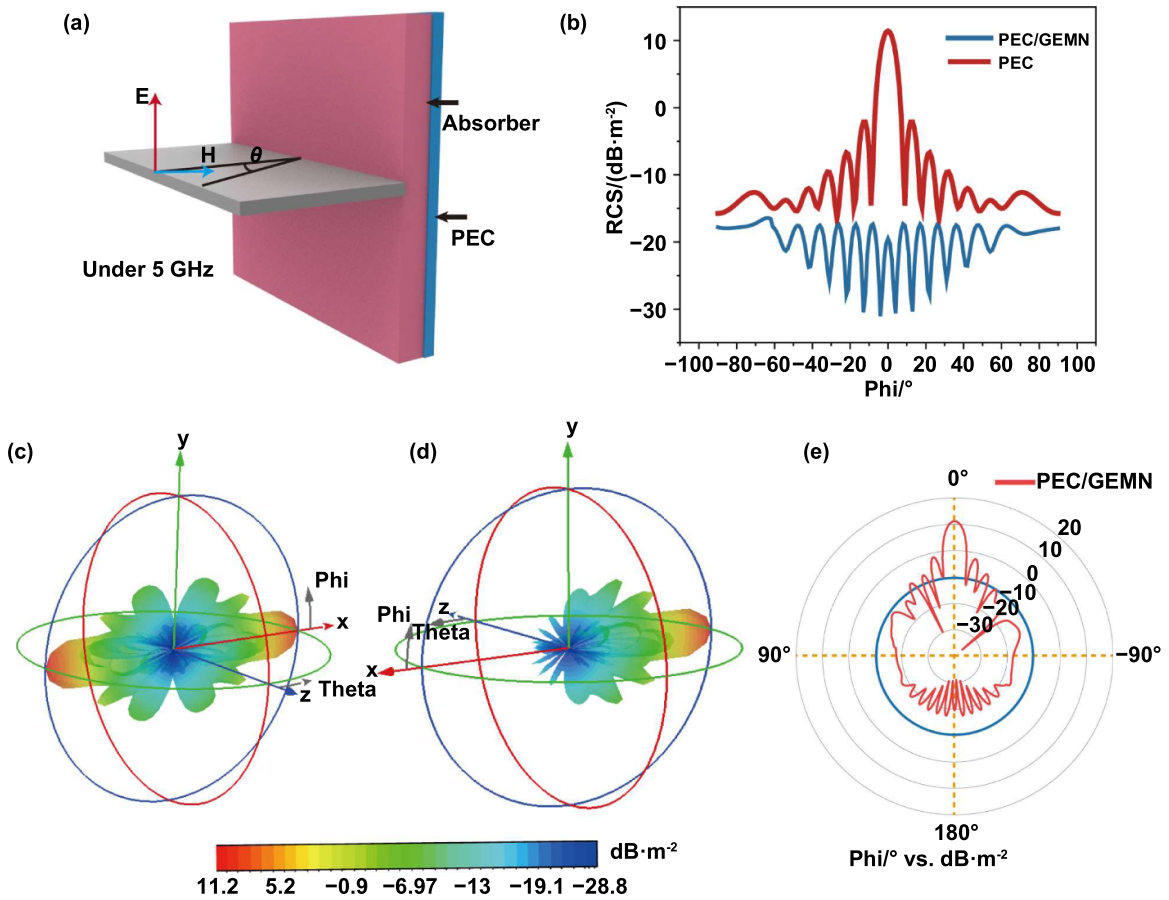


Figure 6. The CST simulation model of RCS with GEMN absorber. (a) The schematic diagram of RCS model. (b) Simulated RCS results of PEC and GEMN(Fe/Co/Ni) covered PEC. 3D RCS plots for (c) PEC and (d) covered with GEMN(Fe/Co/Ni). (e) RCS values of samples at different angles.

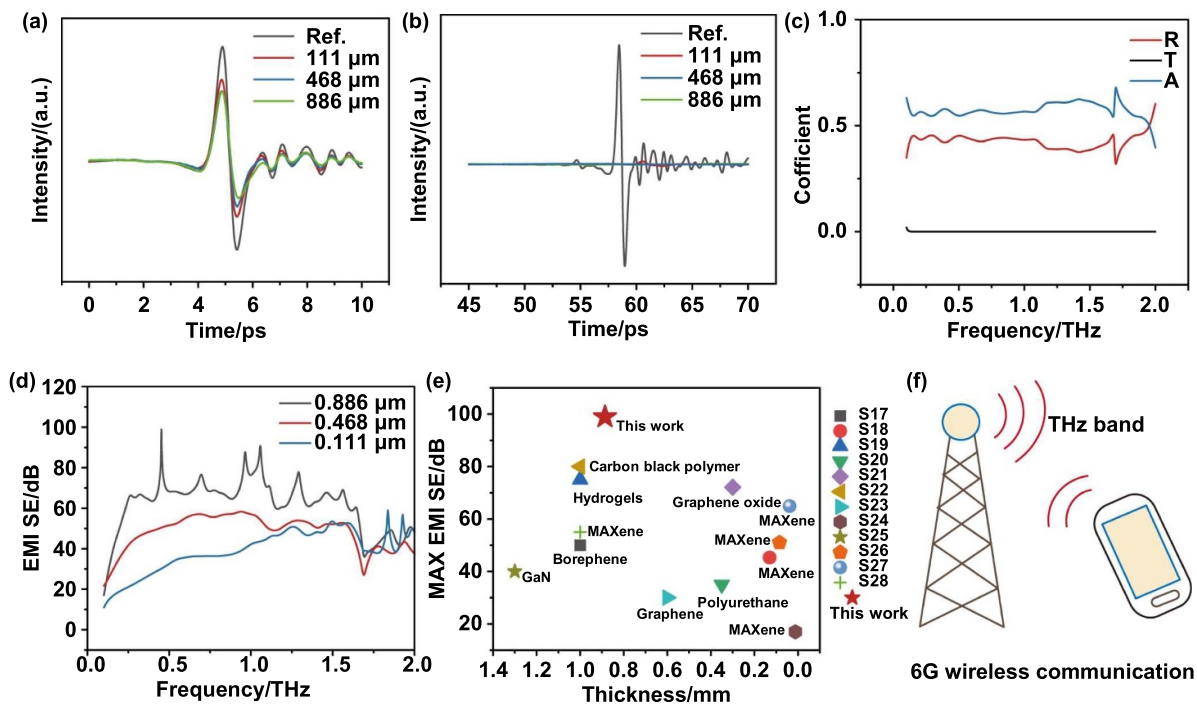


Figure 7. Terahertz absorption performance of the GEMN. The THz testing of the GEMN(Fe/Co/Ni) with air reference (a) reflection consequence and (b) transmission consequence. (c) $A-R-T$ coefficients of the GEMN under THz band. (d) THz shielding performance of GEMN under different thicknesses. (e) The terahertz shielding performance of GEMN and the other class of materials. (f) Schematic of THz-band application in wireless communication.

in THz pollution, giving rise to concerns related to physical health and information security [38]. The demand for efficient THz protective materials has consequently become imperative to address the requirements across diverse frequency bands [23]. The evaluation of THz shielding in this study is predicated on the utilization of both transmission and reflection modes within the framework under the conventional THz time-domain spectroscopy (THz-TDS) system. The reflection mode THz-TDS spectra for the air reference and GEMN(Fe/Co/Ni) samples are presented in figure 7(a). Notably, the reference group exhibits a stronger THz reflection signal due to the complete reflection of THz waves by the aluminum plate. Conversely, the GEMN samples display notably weaker signals, indicating significant penetration of THz waves into the material. In the context of the transmission-mode THz-TDS spectra depicted in figure 7(b), the reference sample allows for the complete passage of THz waves, while the GEMN shows minimal signals, signifying effective THz wave shielding.

According to the $A-R-T$ coefficients of the GEMN under THz band (figure 7(c)), it can be observed that the GEMN exhibits great absorbed performance during the EMW shielding process. Combined with the electromagnetic properties of GEMN, it can be inferred that this behavior arises from the conversion of the highly conductive network into electrical current and heat, thereby dissipating THz energy, and from the intricate porous structure within the film that promotes internal reflection and scattering of THz waves. Figure 7(d) examines the shielding property of GEMN under several thicknesses, which reveals its exceptional THz shielding capability.

The peak shielding value reaches 98.92 dB under $0.886 \mu\text{m}$, and the average shielding result of approximately 55.47 dB is included in the frequency of 0.1–2 THz. This performance vastly outperforms that of other EMI shielding materials, which was detailedly illustrated in figure 7(e). Consequently, owing to its remarkable THz EMI shielding efficacy, GEMN holds immense promise for applications in the realm of 6G technology, as depicted in figure 7(f).

3. Conclusion

In summary, LITEN has been established as a robust approach for the transformation of MTV-MOF into a series of GEMNs, thereby enabling wideband EMW absorption and shielding across GHz and THz ranges. In contrast to alternative carbonization techniques employed in carbon-based MOF derivatization, laser thermal-chemical inducing offers distinct advantages in terms of its rapid, convenient, and straightforward process, thereby demonstrating potential for large-scale production. This methodology facilitates the generation of reduced nanoparticles as small as 3 nm, intricately enclosed within graphene shells. Concurrently, the laser-induced formation of heterojunction microstructures engenders abundant heterointerfaces that potentiate heightened dielectric loss capabilities. Furthermore, the adjustability of the degree of graphitization afforded by this technique enables precise modulation of impedance matching, ultimately contributing to enhanced absorption property. In the microwave range, the synergistic integration of graphene and magnetic nanoalloys, coupled

with high-density magnetic-carbon unit interactions, enables effective impedance matching within the C-band. This configuration yields a noteworthy RL_{\min} with -50.6 dB at 4.98 GHz. This exceptional performance stems from optimized impedance matching under laser parameter control. Expanding into the THz regime, the GEMN exhibits an extraordinary RL_{\max} result of 98.92 dB, accompanied by an extensive frequency scope of 0.1 – 2 THz. This remarkable THz shielding proficiency emanates from the harmonious interplay between excellent electrical conductivity and a porous microstructure. Given its remarkable EMW absorption and shielding prowess across a broad frequency spectrum, the GEMN material, along with its associated preparatory techniques, holds substantial potential for catalyzing advancements in the forthcoming era of wireless communication technologies.

4. Experimental section

4.1. Material

$(\text{Co}(\text{CH}_3\text{COO})_2 \cdot 4\text{H}_2\text{O})$, $(\text{Ni}(\text{CH}_3\text{COO})_2 \cdot 4\text{H}_2\text{O})$, $(\text{Fe}(\text{CH}_3\text{COO})_2 \cdot 4\text{H}_2\text{O})$ and *p*-phthalic acid (1, 4-BDC) were purchased from Sigma Aldrich Corporation. N, N-Dimethylformamide (DMF) was purchased from Shanghai Sinopharm Chemical Reagent. And all reagents were used as received without treatment.

4.2. Synthesis of GEMN

The synthesized method of Fe/Co/Ni MTV-MOF was referenced from Qian *et al* [31]. Take the synthesis of $(\text{Ni}_2\text{Co}_1)_{0.9}\text{Fe}_{0.1}$ -MOF as an example, 0.6 mmol of $\text{Ni}(\text{CH}_3\text{COO})_2 \cdot 4\text{H}_2\text{O}$, 0.3 mmol of $\text{Co}(\text{CH}_3\text{COO})_2 \cdot 4\text{H}_2\text{O}$, and 0.1 mmol $\text{Fe}(\text{CH}_3\text{COO})_2 \cdot 4\text{H}_2\text{O}$ were dissolved in 10 ml DMF. And 1 mmol of 1, 4-dicarboxybenzene was dissolved with 5 ml DMF. Then, solution A was quickly poured into the solution B under magnetic stirring and maintained for 1 h at room temperature. Finally, the products $(\text{Ni}_2\text{Co}_1)_{0.925}\text{Fe}_{0.075}$ -MOF were obtained by centrifugation, washing with DMF and ethanol for several times, and drying at 60 °C for 12 h in electric oven before being used for laser treatment.

Under the laser thermal-chemical inducing, the nanosecond laser system was used for laser source, with 80 ns pulse duration and 1064 nm wavelength at 20 kHz. Here, to obtain the GEMN, the laser power adjusted to 4.56 W with the velocity of 100 $\text{mm}\cdot\text{s}^{-1}$, and the scan interval is 12 μm .

4.3. Material characterization

The morphology and microstructure of the Fe/Co/Ni MOF and GEMN are characterized by SEM (Zeiss SIGMA, Carl Zeiss AG Co. Ltd), TEM (JEOL, Japan), contourgraph (Bruker Countour GTK 3D).

The chemical state of the sample was determined using XPS (Thermo Fisher Scientific). The XRD (XPert Pro) patterns were recorded in the range of 10° – 80° with $2^\circ\cdot\text{min}^{-1}$. FTIR (Thermo Nicolet 5700) spectra of the samples have been further measured. The BET surface area was measured

by (Micromeritics, ASAP2460). And the VSM was measured by the LakeShore7404. The Raman spectra were tested by a 532 nm laser excitation (Raman spectrometer, in Via Reflex).

4.4. Electromagnetic parameters measurement

The electromagnetic parameters were tested by vector network analyzer (Agilent E5071C). The ring-like samples (outer/inner diameters of 7.0 mm/ 3.04 mm) in this study were formed using the transmission/reflection coaxial line method. The GEMN composite was present in the mixture at a weight ratio of 25% , relative to the total mixture. This composition was utilized in the fabrication of the ring-like samples for further analysis or experimentation.

4.5. Microwave absorption calculation

Based on the electromagnetic parameters measured above, the microwave absorption performance was deduced from following equations through the transmission line theory,

$$Z_{\text{in}} = Z_0 \sqrt{\frac{u_r}{e_r}} \tanh \left[j \left(\frac{2\pi f d}{c} \right) \sqrt{u_r e_r} \right] \quad (1)$$

$$RL \text{ (dB)} = 20 \log \left| \frac{z_{\text{in}} - z_0}{z_{\text{in}} + z_0} \right| \quad (2)$$

where Z_{in} represents the input characteristic impedance; Z_0 represents the free space impedance; u_r and e_r are the complex permeability and permittivity; d represents the sample thickness; c represents the velocity of microwave; and f represents the frequency of the corresponding band.

4.6. THz shielding and absorption measurements

Analysis of GEMN shielding performance in THz band was using THz-TDS system. The testing frequency scope is 0.1 – 2 THz, and the EMI shielding performance can be inferred by these equations:

$$\text{EMI SE} = -20 \log (E_s/E_a) \quad (3)$$

E_s and E_a represent the amplitudes of THz pulses for the samples and the air cavity, respectively. In addition, the RL values of the sample can be inferred from this equation:

$$RL = -20 \log (E_i/E_r) \quad (4)$$

E_i and E_r represent the amplitudes of reflection THz pulses for the samples and the reference Al plate, respectively.

Acknowledgments

We thank the support from the Test Center and the Large-scale Instrument and Equipment of Wuhan University.

ORCID iD

Gary J Cheng  <https://orcid.org/0000-0002-1184-2946>

References

- [1] Iqbal A, Shahzad F, Hantanasirisakul K, Kim M K, Kwon J, Hong J, Kim H, Kim D, Gogotsi Y and Koo C M 2020 Anomalous absorption of electromagnetic waves by 2D transition metal carbonitride Ti_3CNT_x (MXene) *Science* **369** 446–50
- [2] Alsharif M H and Nordin R 2017 Evolution towards fifth generation (5G) wireless networks: current trends and challenges in the deployment of millimetre wave, massive MIMO, and small cells *Telecommun. Syst.* **64** 617–37
- [3] Li S C, Xu L D and Zhao S S 2015 The internet of things: a survey *Inf. Syst. Front.* **17** 243–59
- [4] Nguyen D C, Ding M, Pathirana P N, Seneviratne A, Li J, Niyato D, Dobre O and Poor H V 2021 6G internet of things: a comprehensive survey *IEEE Internet Things J.* **9** 359–83
- [5] Chowdhury M Z, Shahjalal M, Ahmed S and Jang Y M 2020 6G wireless communication systems: applications, requirements, technologies, challenges, and research directions *IEEE Open J. Commun. Soc.* **1** 957–75
- [6] Dang S P, Amin O, Shihada B and Alouini M S 2020 What should 6G be? *Nat. Electron.* **3** 20–29
- [7] Nagatsuma T, Ducournau G and Renaud C C 2016 Advances in terahertz communications accelerated by photonics *Nat. Photon.* **10** 371–9
- [8] Yang P, Xiao Y, Xiao M and Li S Q 2019 6G wireless communications: vision and potential techniques *IEEE Netw.* **33** 70–75
- [9] Wang F Y, Li X Z, Chen Z H, Yu W, Loh K P, Zhong B, Shi Y M and Xu Q H 2021 Efficient low-frequency microwave absorption and solar evaporation properties of γ - Fe_2O_3 nanocubes/graphene composites *Biochem. Eng. J.* **405** 126676
- [10] Yang B T, Fang J F, Xu C Y, Cao H, Zhang R X, Zhao B, Huang M Q, Wang X Y, Lv H L and Che R C 2022 One-dimensional magnetic FeCoNi alloy toward low-frequency electromagnetic wave absorption *Nano-Micro Lett.* **14** 170
- [11] Wang B L, Chen H Y, Wang S, Shi Y, Liu X D, Fu Y G and Liu T 2021 Construction of core-shell structured $Co_7Fe_3@C$ nanocapsules with strong wideband microwave absorption at ultra-thin thickness *Carbon* **184** 223–31
- [12] Wan H J, Liu N, Tang J, Wen Q Y and Xiao X 2021 Substrate-independent $Ti_3C_2T_x$ MXene waterborne paint for terahertz absorption and shielding *ACS Nano* **15** 13646–52
- [13] Lv H L, Yang Z H, Wang P L, Ji G B, Song J Z, Zheng L R, Zeng H B and Xu Z J 2018 A voltage-boosting strategy enabling a low-frequency, flexible electromagnetic wave absorption device *Adv. Mater.* **30** 1706343
- [14] Rao L J, Wang L, Yang C D, Zhang R X, Zhang J C, Liang C Y and Che R C 2023 Confined diffusion strategy for customizing magnetic coupling spaces to enhance low-frequency electromagnetic wave absorption *Adv. Funct. Mater.* **33** 2213258
- [15] Cheng Z, Cao Y S, Wang R F, Liu X Y, Fan F and Huang Y 2023 Multifunctional MXene-based composite films with simultaneous terahertz/gigahertz wave shielding performance for future 6G communication *J. Mater. Chem. A* **11** 5593–605
- [16] Shu J C, Cao W Q and Cao M S 2021 Diverse metal–organic framework architectures for electromagnetic absorbers and shielding *Adv. Funct. Mater.* **31** 2100470
- [17] Liu P B, Gao S, Zhang G Z, Huang Y, You W B and Che R C 2021 Hollow engineering to Co@N-doped carbon nanocages via synergistic protecting-etching strategy for ultrahigh microwave absorption *Adv. Funct. Mater.* **31** 2102812
- [18] Li H L, Eddaoudi M, O’Keeffe M and Yaghi O M 1999 Design and synthesis of an exceptionally stable and highly porous metal–organic framework *Nature* **402** 276–9
- [19] Nicks J, Sasitharan K, Prasad R R R, Ashworth D J and Foster J A 2021 Metal–organic framework nanosheets: programmable 2D materials for catalysis, sensing, electronics, and separation applications *Adv. Funct. Mater.* **31** 2103723
- [20] Zhang X et al 2023 Conductive metal–organic frameworks with tunable dielectric properties for boosting electromagnetic wave absorption *ACS Nano* **17** 12510–8
- [21] Ren Y J, Wang X, Ma J X, Zheng Q, Wang L J and Jiang W 2023 Technology, metal–organic framework-derived carbon-based composites for electromagnetic wave absorption: dimension design and morphology regulation *J. Mater. Sci. Technol.* **132** 223–51
- [22] Ferguson B and Zhang X C 2002 Materials for terahertz science and technology *Nat. Mater.* **1** 26–33
- [23] Pavlou C, Pastore Carbone M G, Manikas A C, Trakakis G, Koral C, Papari G, Andreone A and Galiotis C 2021 Effective EMI shielding behaviour of thin graphene/PMMA nanolaminates in the THz range *Nat. Commun.* **12** 4655
- [24] Jiang H Q, Jin S Y, Wang C, Ma R Q, Song Y Y, Gao M Y, Liu X T, Shen A G, Cheng G J and Deng H X 2019 Nanoscale laser metallurgy and patterning in air using MOFs *J. Am. Chem. Soc.* **141** 5481–9
- [25] Cao Y S, Cheng Z, Wang R F, Liu X Y, Zhang T R, Fan F and Huang Y 2022 Multifunctional graphene/carbon fiber aerogels toward compatible electromagnetic wave absorption and shielding in gigahertz and terahertz bands with optimized radar cross section *Carbon* **199** 333–46
- [26] Wu F, Li Q, Liu Z H, Shah T, Ahmad M, Zhang Q Y and Zhang B L 2021 Fabrication of binary MOF-derived hybrid nanoflowers via selective assembly and their microwave absorbing properties *Carbon* **182** 484–96
- [27] Liu Y, Zhou X F, Jia Z R, Wu H J and Wu G J 2022 Oxygen vacancy-induced dielectric polarization prevails in the electromagnetic wave-absorbing mechanism for Mn-based MOFs-derived composites *Adv. Funct. Mater.* **32** 2204499
- [28] Ouyang J, He Z L, Zhang Y, Yang H M and Zhao Q H 2019 Trimetallic FeCoNi@C nanocomposite hollow spheres derived from metal–organic frameworks with superior electromagnetic wave absorption ability *ACS Appl. Mater. Interfaces* **11** 39304–14
- [29] Yi P S, Zhang X F, Jin L Q, Chen P, Tao J Q, Zhou J T and Yao Z J 2022 Regulating pyrolysis strategy to construct CNTs-linked porous cubic Prussian blue analogue derivatives for lightweight and broadband microwave absorption *Biochem. Eng. J.* **430** 132879
- [30] Li Y X, Liao Y J, Ji L Z, Hu C L, Zhang Z H, Zhang Z Y, Zhao R Z, Rong H W, Qin G W and Zhang X F 2022 Quinary high-entropy-alloy@graphite nanocapsules with tunable interfacial impedance matching for optimizing microwave absorption *Small* **18** 2107265
- [31] Qian Q Z, Li Y P, Liu Y, Yu L and Zhang G Q 2019 Ambient fast synthesis and active sites deciphering of hierarchical foam-like trimetal–organic framework nanostructures as a platform for highly efficient oxygen evolution electrocatalysis *Adv. Mater.* **31** 1901139
- [32] Jing Y Q, Qu J, Jia X Q, Zhai X Z, Chang W, Zeng M J, Li X F and Yu Z Z 2021 Constructing tunable core-shell $Co_5Ge_3@Co$ nanoparticles on reduced graphene oxide by an interfacial bonding promoted Kirkendall effect for high lithium storage performances *Biochem. Eng. J.* **408** 127266
- [33] Jia L, Wang D H, Huang Y X, Xu A W and Yu H Q 2011 Highly durable N-doped graphene/CdS nanocomposites with enhanced photocatalytic hydrogen evolution from water under visible light irradiation *J. Phys. Chem. C* **115** 11466–73

- [34] Shen J Y, Zhang D F, Han C, Wang Y, Zeng G X and Zhang H Y 2021 Three-dimensional flower-like FeCoNi/reduced graphene oxide nanosheets with enhanced impedance matching for high-performance electromagnetic wave absorption *J. Alloys Compd.* **883** 160877
- [35] Ma Z, Cao C T, Liu Q F and Wang J B 2012 A new method to calculate the degree of electromagnetic impedance matching in one-layer microwave absorbers *Chin. Phys. Lett.* **29** 038401
- [36] Zhou Y K, He P, Ma W J, Zuo P Y, Xu J, Tang C H and Zhuang Q X 2024 The developed wave cancellation theory contributing to understand wave absorption mechanism of ZIF derivatives with controllable electromagnetic parameters *Small* **20** 2305277
- [37] Xu H X, Zhang G Z, Wang Y, Ning M Q, Ouyang B, Zhao Y, Huang Y and Liu P B 2022 Size-dependent oxidation-induced phase engineering for MOFs derivatives via spatial confinement strategy toward enhanced microwave absorption *Nano-Micro Lett.* **14** 102
- [38] Bai Y, Qin F and Lu Y X 2022 Lightweight Ni/CNT decorated melamine sponge with sensitive strain sensing performance for ultrahigh electromagnetic absorption in both GHz and THz bands *Biochem. Eng. J.* **429** 132393